RSC Advances

PAPER

View Article Online
View Journal | View Issue

Cite this: *RSC Adv.*, 2020, **10**, 9917

Synthesis of a fine $LiNi_{0.88}Co_{0.09}Al_{0.03}O_2$ cathode material for lithium-ion batteries *via* a solvothermal route and its improved high-temperature cyclic performance

Guolin Cao,†[ab] Jie Zhu,†[a] Yunjiao Li,* [a] Yuan Zhou,[c] Zhuomin Jin,[b] Bin Xu,[b] Chunxi Hai [c] and Jinbo Zeng[c]

Received 16th October 2019
Accepted 7th January 2020

DOI: 10.1039/c9ra08450a

rsc.li/rsc-advances

Nickel–Cobalt–Aluminum (NCA) cathode materials for lithium-ion batteries (LIBs) are conventionally synthesized by chemical co-precipitation. However, the co-precipitation of Ni^{2+}, Co^{2+}, and Al^{3+} is difficult to control because the three ions have different solubility product constants. This study proposes a new synthetic route of NCA, which allows fabrication of fine and well-constructed NCA cathode materials by a high temperature solid-state reaction assisted by a fast solvothermal process. The capacity of the $LiNi_{0.88}Co_{0.09}Al_{0.03}O_2$ as-synthesized by the solvothermal method was 154.6 mA h g^{-1} at 55 °C after 100 cycles, corresponding to 75.93% retention. In comparison, NCA prepared by the co-precipitation method delivered only 130.3 mA h g^{-1} after 100 cycles, with a retention of 63.31%. Therefore, the fast solvothermal process-assisted high temperature solid-state method is a promising candidate for synthesizing high-performance NCA cathode materials.

1. Introduction

Current improvements in electric vehicles and large-scale energy storage systems have greatly raised the demand for rechargeable batteries with high energy density, and this trend is expected to continue over the next few years.[1–5] Therefore, it is necessary to develop new cathode materials with high capacity and safety.[6–8] Great efforts have been made toward the synthesis of nickel rich layered cathode materials. Nickel–Cobalt–Aluminum (NCA) is characterized by high reversible capacity, long cycle life and a high operating potential (3.6 V *vs.* Li^+/Li), which are desired properties of cathode materials for lithium-ion batteries.[9] At present, NCA cathode materials are fabricated by one of two main synthetic routes. In one route, the NCA precursor is synthesized by a co-precipitation method, and the NCA cathode material is then obtained by high-temperature lithiation of the precursor. This method is the present-day mainstream synthesis pathway of NCA. However, the co-precipitation of Ni^{2+}, Co^{2+}, and Al^{3+}, and the uniformity of the particle size are difficult to control because the solubility product constants of $Ni(OH)_2$, $Co(OH)_2$ and $Al(OH)_3$ are largely different ($k_{sp}{}^{\theta} = 5.0 \times 10^{-16}$, 2.3×10^{-16}, 1.3×10^{-23}, respectively). This problem has blocked the large-scale application of NCA.[10,11] In the second synthesis method, Ni–Co precursor synthesized by the co-precipitation method is thoroughly mixed with Al source (nanosized Al_2O_3 or $Al(OH)_3$) and LiOH. This mixed powder is sintered at high temperature to obtain the NCA cathode material. However, the NCA prepared by this route is degraded by uneven distribution of the Al elements caused by the limited solid-phase diffusion, and surface passivation caused by the excessive inert Al-containing surface layer. These defects reduce the electrochemical performance of the synthesized NCA.

In recent years, the solvothermal method has become a popular synthesis route for advanced functional materials.[12–15] The solvothermal synthesis of binary metal oxides as anode materials for lithium-ion batteries (LIBs) (*e.g.*, $NiCo_2O_4$, $CoMoO_4$, $MnCo_2O_4$, and $ZnCo_2O_4$) has aroused public attention.[11,13,16–19] However, few studies have applied the solvothermal method to the fabrication of candidate NCA cathode materials for LIBs. Compared with other synthesis methods (*e.g.*, spray pyrolysis[20,21] and co-precipitation[22–24]), the solvothermal method achieves functional materials with good crystallinity and high purity at low cost. In this study, an NCA precursor comprising uniformly dispersed Ni–Co microspheres (named $Ni_{0.91}Co_{0.09}$ microspheres) with fine size and a large Brunauer–Emmett–Teller (BET) surface area was synthesized using the solvothermal method. Subsequently, the feasibility of $LiNi_{0.88}Co_{0.09}Al_{0.03}O_2$ based on $Ni_{0.91}Co_{0.09}$ microsphere

[a]School of Metallurgy and Environment, Central South University, Changsha 410083, P. R. China. E-mail: yunjiao_li@csu.edu.cn

[b]Qing Hai Kuai Lv High-tech Co., Ltd, Xining 810008, P. R. China

[c]Key Laboratory of Comprehensive and Highly Efficient Utilization of Salt Lake Resources, Qinghai Institute of Salt Lakes, Chinese Academy of Sciences, Xining 810008, P. R. China

† The two authors contributed equally to this paper.

precursors was adopted as the cathode material of LIBs, and its improved high-temperature cyclic performance was verified in electrochemical tests.

2. Experimental section

2.1. Synthesis of the materials

All chemicals were of analytical grade and provided by Aladdin (Shanghai) Co., Ltd (Shanghai, China). Fig. 1a shows the preparation of the $Ni_{0.91}Co_{0.09}$ microsphere precursor by the solvothermal method. First, stoichiometric $Ni(NO_3)_2$ and $Co(NO_3)_2$ with a Ni/Co molar ratio of 0.91 : 0.09 (concentration = 0.1 mol L^{-1}) were dissolved in 150 mL absolute ethanol, yielding a clear dark-green solution. The resulting solution was transferred to a 150 mL Teflon-lined autoclave and heated for 12 h at 180 °C. After naturally cooling the solution to room temperature, we collected the yellow-green precipitate and washed it several times with absolute ethanol. The washed precipitate was dried for 8 h at 100 °C in a vacuum oven, yielding the Ni–Co microsphere precursor (marked as S-NC). As a comparison material, we purchased the co-precipitation precursor $Ni_{0.88}Co_{0.09}Al_{0.03}(OH)_2$ (named C-NC) from Qing Hai Kuai Lv High-tech Co., Ltd.

To prepare the NCA cathode material, the $Ni_{0.91}Co_{0.09}$ microsphere precursors were thoroughly mixed with $LiOH \cdot H_2O$ micropowder and nano-$Al(OH)_3$ (the molar ratio of Li : Me : Al (Me = Ni, Co) reached 1.05 : 0.97 : 0.03). Subsequently, the $LiNi_{0.88}Co_{0.09}Al_{0.03}O_2$ cathode material (S-NCA) was synthesized by pre-treating the mixed powder for 5 h at 480 °C, followed by 12 h sintering at 750 °C in a pure O_2 atmosphere. As a comparison cathode, we purchased commercial $LiNi_{0.88}Co_{0.09}Al_{0.03}O_2$ cathode material (C-NCA) based on the C-NC precursor from Qing Hai Kuai Lv High-tech Co., Ltd.

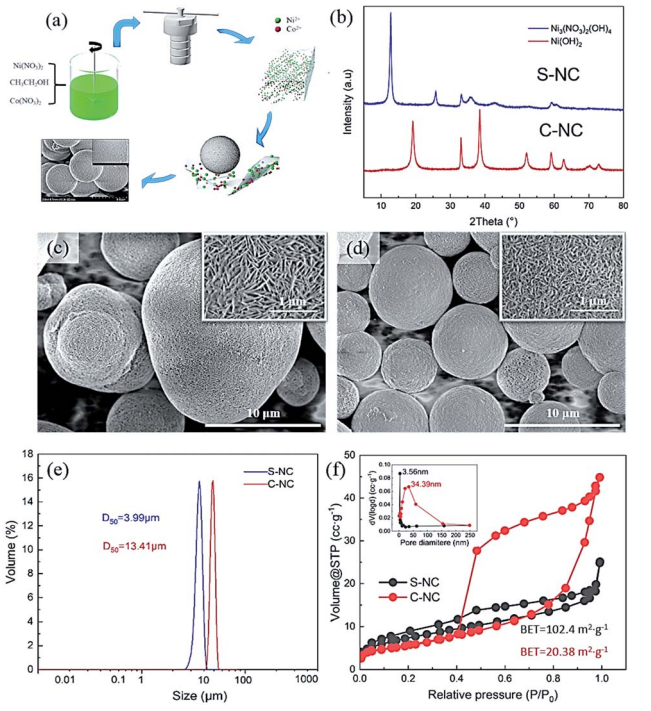

Fig. 1 (a) Schematic illustration for preparation of S-NC; (b) X-ray diffraction (XRD) patterns of the as-prepared precursors; field emission scanning electron microscope (FESEM) images: (c) C-NC and (d) S-NC; (e) particle-size distribution of the precursors; (f) N_2 adsorption/desorption isotherm curves and corresponding distribution of pore size (inset) exhibited by the precursors. D_{50} denotes median particle size.

2.2. Material characterization

The sample phases were characterized by powder X-ray diffraction (XRD; Rigaku, D/max-2500) with Cu Kα radiation (λ = 1.5418 Å). The XRD dates were collected over the 2θ range 10–80° at a scanning rate of 2° min^{-1}. The sample morphologies and their element distributions were observed under a field emission scanning electron microscope (FESEM; SU8010) outfitted with X-MAXN energy-dispersive spectroscopy. The microelements in the samples, such as lithium, nickel, cobalt, and aluminum, were verified by inductively coupled plasma spectroscopy (ICP; PerkinElmer, Optima 2100 DV). Table 1 lists the elemental compositions of the as-prepared samples detected by ICP. The specific surface areas and porosities of the precursors at 77 K were measured from the N_2 adsorption/desorption isotherms acquired by a Micrometrics ASAP 2020M system. The particle-size distributions in the materials were measured by a laser analyzer (Malvern 3000). Surface analysis was performed by X-ray photoelectron spectroscopy (XPS, PHI5600, PerkinElmer).

2.3. Electrochemical testing

The prepared NCA powder was fully mixed with polyvinylidene fluoride and acetylene carbon black at a weight ratio of 8 : 1 : 1. The mixed powder was dispersed in *N*-methyl-2-pyrrolidone, then pasted onto the aluminum foil of the collector as the working electrode. This preparation was dried overnight at 90 °C in a vacuum oven. We assembled the CR2016 type coin cells in a glove-box filled with argon (LS800S, DELLIS) with the Celgard-2400, the metallic lithium and the 1 M $LiPF_6$ in EC : DMC : EMC (volume ratio of 1 : 1 : 1) as the separator, the counter electrode, and the electrolyte, respectively. Charge/discharge experiments were performed on a LAND test system (CT2001A, Wuhan LAND electronics Co., Ltd.) at different rates (1C = 180 mA h g^{-1} over 3.0–4.3 V *vs.* Li/Li^+). Cyclic voltammetry (CV) was implemented on an electrochemical workstation (Applied Research, Princeton) at a scan rate of 0.1 mV s^{-1}. The impedances were measured several times with a computer-controlled CHI instrument operated at room temperature. The frequency was reduced from 100 kHz to 0.01 Hz at an AC signal amplitude of ±10 mV. As for the analysis of differential scanning calorimetry (DSC), the 2016 coin-type cells were fully charged to 4.3 V at 55 °C and dismantled in an Ar-filled glove box. After the remaining electrolyte was carefully removed from the surface of the electrode, the cathode materials were recovered from the current collector. We collect about 5 mg samples using a stainless steel sealed pan with a gold-plated copper seal. The measurement above were performed in a DSC Q2000 (TA, America) at a temperature scan rate of 5 °C min^{-1}.

Table 1 The elemental compositions of the as-prepared samples

Sample	Li (mol g^{-1})	Ni (mol g^{-1})	Co (mol g^{-1})	Al (mol g^{-1})	Mole ratio
C-NC	0	0.0096	0.0010	0.0003	Ni : Co : Al, 0.88 : 0.09 : 0.03
S-NC	0	0.0073	0.0007	0	Ni : Co : Al, 0.91 : 0.09 : 0.00
C-NCA	0.0108	0.0095	0.0010	0.0003	Li/Me (Ni : Co : Al), 1.00 (0.88 : 0.09 : 0.03)
S-NCA	0.0109	0.0097	0.0010	0.0003	Li/Me (Ni : Co : Al), 0.99 (0.88 : 0.09 : 0.03)

3. Results and discussion

Fig. 1b shows the XRD patterns of the $Ni_{0.91}Co_{0.09}$ microspheres and $Ni_{0.88}Co_{0.09}Al_{0.03}(OH)_2$ precursor. The XRD peaks of S-NC and C-NC were identified as $Ni_3(NO_3)_2{\cdot}(OH)_4$ (PDF#25-0752) and $Ni(OH)_2$ (PDF#14-0117), respectively, confirming the purity of the samples. The formation mechanism of $Ni_3(NO_3)_2{\cdot}(OH)_4$ was not co-precipitation, but was interpreted as follows:[16]

$$7CH_3CH_2OH + 4NO_3^- \rightarrow 7CH_3CHO + 2NO\uparrow + N_2O\uparrow + 4OH^- + 5H_2O \quad (1)$$

$$3Ni^{2+} + 2NO_3^- + 4OH^- \rightarrow Ni_3(NO_3)_2(OH)_4 \quad (2)$$

Fig. 1c and d show the morphologies of S-NC and C-NC, respectively. Both precursors exhibited their spherical forms and regular needle-like nanorod primary particles, but the S-NC appeared to contain more regular and uniformly sized spheres than C-NC. The particle-size distributions (Fig. 1e) of both precursors further verified the finer particles in S-NC ($D_{50} = 3.99$ μm) than in C-NC ($D_{50} = 13.41$ μm). Fig. 1f plots the N_2 adsorption/desorption isotherm curves and pore-size distributions (inset) in the precursors. Both precursors yielded a type-IV isotherm, but C-NC exhibited H4 hysteresis loops which were absent in S-NC. This result indicates a significant difference between the pore-size distributions of S-NC and C-NC. In fact, the pore-size distribution in S-NC was narrow and centered at 3.56 nm, whereas that of C-NC was wide (10–150 nm) and centered at 34.39 nm (Fig. 1f, inset). Furthermore, the BET surface area was larger in S-NC than in C-NC (102.4 $m^2\ g^{-1}$ *versus* 20.38 $m^2\ g^{-1}$).

Fig. 2 displays the XRD patterns of C-NCA and S-NCA. The diffraction peaks exhibit a typical layered structure belonging to $LiNiO_2$ (LNO) with a space group of $R\bar{3}m$, consistent with the standard cards (PDF#09-0063). The $I(003)/I(104)$ and c/a ratios were larger in S-NCA than in C-NCA, indicating a well-ordered layered structure of S-NCA.[25,26] Based on this structural information, the high temperature solid-state method assisted by the solvothermal process can synthesize well-ordered Ni-rich layered NCA cathode materials. Panels a and b of Fig. 3 display the FESEM images of the C-NCA and S-NCA cathode materials, respectively. The as-synthesized $LiNi_{0.88}Co_{0.09}Al_{0.02}O_2$ cathode materials inherited the sphere-like morphology and particle sizes of their respective precursors, but the high-temperature calcination made a rough surface due to the precursor decomposition and solid-state reactions. Careful inspection of the FESEM images reveals both smaller secondary particles and denser primary particles in S-NCA than in C-NCA. Fig. 3c and d show cross-sectional images of the NCAs and their corresponding EDS mappings, respectively. Clearly, S-NCA possessed a more compact bulk structure than C-NCA. The cross-section EDS mapping results verified the even distributions of Ni, Co, and Al in the particle bulks for S-NCA.

The chemical composition and oxidation states of the NCA cathode materials were further elucidated in XPS measurements. The survey spectrum in Fig. 4a reveals the existence of Ni, Co, Al, O, and C near the surfaces of the samples. The C may originate from adventitious hydrocarbons in the analysis chamber.[26] Fig. 4b shows the Ni 2p spectra and their fitting curves. The deconvoluted peaks at binding energies of ≈855.5 and 872.4 eV were assignable to Ni $2p_{3/2}$ and Ni $2p_{1/2}$, respectively. The binding energy difference between Ni $2p_{3/2}$ and Ni $2p_{1/2}$ (Ni, DS-2p) was well matched to the doublet separation of Ni^{2+}.[27] Meanwhile, the DS-2p of 17.6 eV ($2p_{1/2}$–$2p_{3/2}$) indicated the existence of Ni^{3+} in both samples.[27,28] From the areas of the deconvolved peaks, the Ni^{2+}/Ni^{3+} ratios in S-NCA and C-NCA were determined as 2.32 : 7.68 and 3.79 : 6.21, respectively. Obviously, the Ni^{3+} content of the surface layer was higher in S-NCA than in C-NCA. The S-NC precursor with a large specific surface area could maximize the contact area between the precursor and LiOH, facilitating the transformation of Ni^{2+} into Ni^{3+} during the sintering process.[21] Ultimately, the Ni^{3+}-rich S-NCA yielded a well-ordered layered $LiNiO_2$-based cathode material with a low Li/Ni mixing degree and a stable structure.

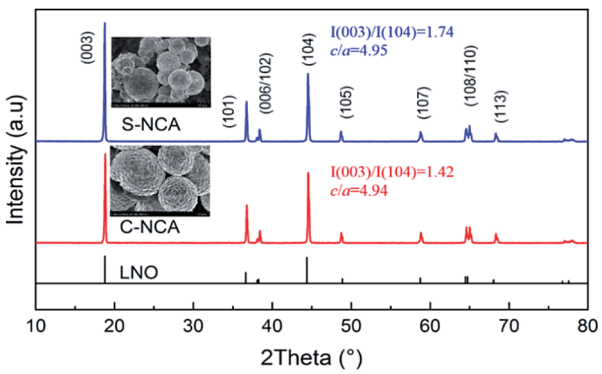

Fig. 2 XRD patterns of the NCAs prepared by the solvothermal route and co-precipitation route, respectively.

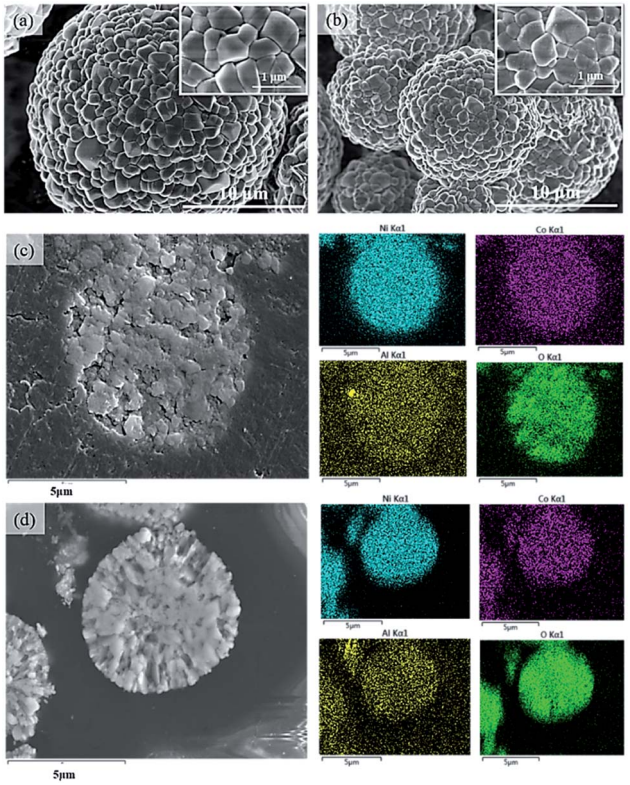

Fig. 3 FESEM images presented by C-NCA (a) and S-NCA (b); cross-section images presented by C-NCA (c) and S-NCA (d) with corresponding EDS mapping.

The electrochemical performances of C-NCA and S-NCA were shown in Fig. 5. The both NCAs exhibited similar initial charge–discharge profiles at 0.1C and 3.0–4.3 V (see Fig. 5a), suggesting the same charge–discharge mechanism in the two materials. The initial discharge capacities of S-NCA and C-NCA were 210.7 and 203.2 mA h g^{-1}, with coulombic efficiencies of 83.21% and 80.25%, respectively. Fig. 5b shows the cyclabilities of S-NCA and C-NCA at room temperature. Both NCAs exhibited almost identical capacity retentions (~87%) after 100 cycles at 1C, and almost identical capacities at different current densities (Fig. 5c). Obviously, the electrochemical performance of S-NCA was similar to that of C-NCA at room temperature. However, as

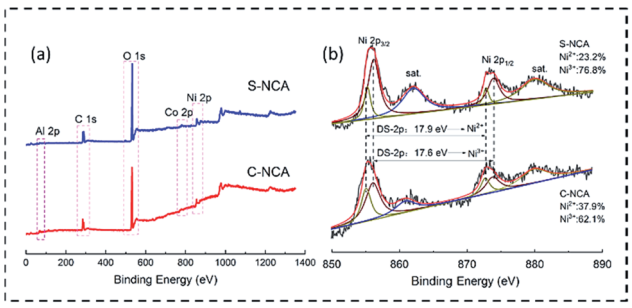

Fig. 4 XPS spectra of C-NCM and S-NCA: (a) survey spectrum; (b) Ni 2p.

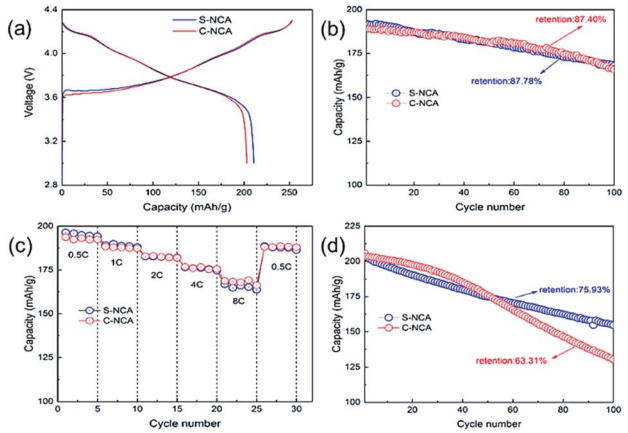

Fig. 5 Electrochemical performances of C-NCA and S-NCA: (a) initial charge–discharge curves at 0.1C; (b) cycling performance at 1C; (c) rate capabilities; (d) cycling performance at 55 °C.

demonstrated in the high-temperature cycling performances of the NCA samples (Fig. 5d), the S-NCA delivered outstanding cycling performance at 55 °C. At the raised temperature, the capacity of S-NCA was 154.6 mA h g^{-1} after 100 cycles, corresponding to a retention capacity of 75.93%. In comparison, the C-NCA delivered only 130.3 mA h g^{-1} after 100 cycles at 55 °C (capacity retention = 63.31%).

The kinetic processes of the electrodes reactions at 55 °C were investigated by CV. The results are shown in Fig. 6. Both NCAs present the same three pairs of redox peaks. The peak currents of the redox reactions weakened with cycling, revealing that the capacity degraded during the charge–discharge process. The paired peaks in the CV curves are assignable to the three phase transformations (H1 ↔ M, M ↔ H2, H2 ↔ H3) in $LiNiO_2$-based cathode materials during charge–discharge.[25,29–31] The potential difference (ΔE) between the major redox couples in the CV cycles usually specifies the reference point of the polarization degree.[32–34] As shown in Fig. 4, the ΔE values were higher in C-NCA ($\Delta E_1 = 230$ mV, $\Delta E_{100} = 130$ mV) than in S-NCA ($\Delta E_1 = 190$ mV, $\Delta E_{100} = 100$ mV), suggesting that polarization in S-NCA was inhibited at elevated temperature. The enhanced polarization and accelerated electrolyte decomposition causes the rapid capacity decay in C-NCA batteries at high temperature. The S-NCA synthesized by the solvothermal routine exhibited a finer size and more uniform particle-size distribution than C-

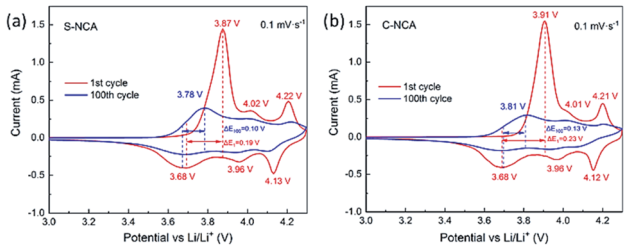

Fig. 6 CV curves with scan rate reaching 0.1 mV s^{-1} at 55 °C: (a) S-NCA; (b) C-NCA.

NCA synthesized by the standard method. These physical refinements shorten the Li^+ diffusion pathways and enhance wettability by the electrolyte,[35,36] thereby inhibiting polarization. Furthermore, the high density of primary particles in S-NCA discourages corrosion of the active material by the electrolyte, as fewer particles are exposed to the electrolyte.

The thermal stabilities of electrochemically delithiated wet $LiNi_{0.88}Co_{0.09}Al_{0.03}O_2$ electrodes were evaluated by differential scanning calorimetry (DSC). As can be seen in Fig. 7, the temperature of S-NCA exothermic peak is significantly higher than that of C-NCA, 234 °C and 178.7 J g^{-1} for S-NCA, 217 °C and 308 J g^{-1} for C-NCA respectively. Notably, C-NCA have poor thermal stabilities. We believe that higher thermodynamics stability is beneficial to the improvement of electrochemical performance.

Next, we studied the structural stability of the NCA cathode materials against electrochemical cycling at elevated temperature. Fig. 8a compares the XRD patterns of the NCA electrodes after 100 cycles at 55 °C. The XRD patterns of both cycled electrodes were consistent with the hexagonal α-$NaFeO_2$ layered structure. However, the half widths of the characteristic peaks were obviously widened after 100 cycles, and the diffraction peaks were weakened (*cf.* the XRD patterns of as-prepared NCA cathode in Fig. 2). Moreover, the 006/102 and 108/110 splitting peaks in the XRD patterns tended to disappear after cycling. The above evidences reveal that the NCA cathode materials were structurally degraded by the high-temperature cycles. However, the diffraction-peak strength and intensity ratio $I(003)/I(104)$ were significantly higher for the S-NCA electrode than for the C-NCA electrode, indicating the higher structural stability and high-temperature cyclic performance of S-NCA than C-NCA.[37,38]

Panels b–d of Fig. 8 show the morphologies of the cycled electrodes at 55 °C. The secondary particles of the S-NCA electrode maintained their spherical shapes at high temperature, even after many cycles (Fig. 8b). Moreover, the primary particles in the S-NCA electrode were compactly stacked with few pulverized and cracking phenomena. In contrast, many hollow shells were observed in the C-NCA electrode (Fig. 8c and d), indicating drastic transition-metal dissolution (TMD) in the C-NCA electrode, and irreversible loss of the active material. TMD is considered as an inevitable defect of TM-containing cathode materials, and is accelerated by elevated temperature and high cut-off voltage.[39,40] TMD is caused by HF generated by the hydrolysis of $LiFP_6$-containing electrolytes, which initiates the reaction $Ni^{2+} + 2F^- \rightarrow NiF_2$.[40–42] The stable well-ordered structure and reduced Ni^{2+} content of the surface in C-NCA effectively alleviates the TMD and loss of active material, thereby conferring excellent high-temperature cyclic performance.

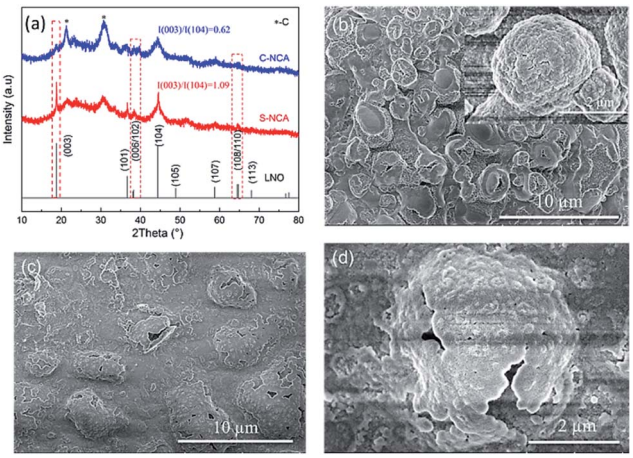

Fig. 8 (a) XRD patterns of the cycled electrodes after 100 cycles at 55 °C; FESEM images of the cycled electrodes after 100 cycles at 55 °C: (b) S-NCA; (c and d) C-NCA.

The difference in capacity fading between the S-NCA and C-NCA materials was further investigated in an electrochemical impedance spectroscopic (EIS) test (Fig. 9). The EIS was carried out in the 3.0–4.3 V range at 55 °C. The equivalent circuit model (Fig. 9a, inset) is detailed elsewhere.[43] Table 2 lists the fitting results of R_{ct} (charge-transfer impedance) and R_f (interface layer impedance). Clearly, the R_{ct} values were higher in C-NCA than in S-NCA after the first cycle. As the cycles proceeded, the R_{sf} and R_{ct} increased in both materials. Specifically, the R_{ct} of C-NCA increased from 105.33 Ω in the first cycle to 530.74 Ω in the 100th cycle, whereas that of S-NCA increased from 43.92 Ω in cycle 1 to 452.45 Ω in cycle 100. The less significant change in S-

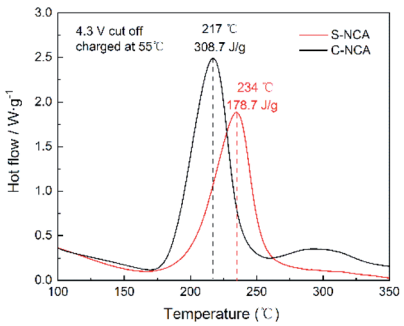

Fig. 7 DSC results of C-NCA and S-NCA.

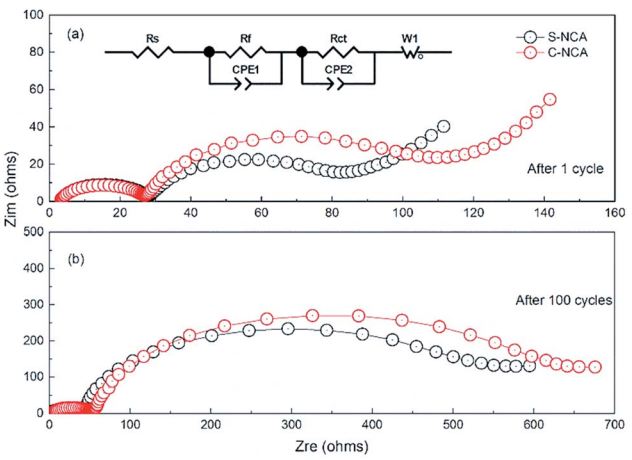

Fig. 9 Nyquist plots of S-NCA and C-NCA electrodes at 55 °C: (a) after 1 cycle; (b) after 100 cycles.

Table 2 The fitted EIS parameters for S-NCA and C-NCA

	After 1st cycle		After 100th cycle	
Sample	R_f (Ω)	R_{ct} (Ω)	R_f (Ω)	R_{ct} (Ω)
S-NCA	16.24	43.92	22.54	452.45
C-NCA	17.38	105.33	25.67	530.74

NCA confirms a more stable electrode–electrolyte interface at elevated temperatures in S-NCA, consistent with the morphological and structural characterizations of the cycled electrodes.

4. Conclusions

In summary, well-constructed fine $LiNi_{0.88}Co_{0.09}Al_{0.03}O_2$ was synthesized as a cathode material for LIBs through the high temperature solid-state reaction assisted by the fast solvothermal process. The NCA cathode material prepared by the solvothermal route (S-NCA) exhibited a finer and more uniform particle size, and denser primary particles, than the NCA material prepared by traditional co-precipitation (C-NCA). The inhibited polarization, stable well-ordered layered structure, and alleviated corrosion of the active material enhanced the initial coulombic efficiency of S-NCA, and boosted its high-temperature cycling performance. This study verifies the possibility of solvothermal NCA synthesis, and may inspire the further investigation and optimization of NCA cathode materials for high-performance LIBs.

Conflicts of interest

There are no conflicts to declare.

Acknowledgements

This work has obtained the support from the Qing Hai Kuai Lv High-tech Co., Ltd and the Science and Technology Department of Guangxi Zhuang Autonomous Region under grant no. 2018AD15002.

References

1 S. Choi, B.-N. Yun, W. D. Jung, T. H. Kim, K.-Y. Chung, J.-W. Son, B.-I. Sang, H.-G. Jung and H. Kim, *Scr. Mater.*, 2019, **165**, 10–14.
2 L. Yang, H. S. Chen, H. Jiang, W. L. Song and D. Fang, *Scr. Mater.*, 2019, **167**, 11–15.
3 J. Zhou, B. Zhao, J. Bai, Z. Fang, K. Li, H. Ma, J. Dai, X. Zhu and Y. Sun, *Scr. Mater.*, 2019, **166**, 87–91.
4 C. Qin, J. Cao, J. Chen, G. Dai, T. Wu, Y. Chen, Y. Tang, A. Li and Y. Chen, *Dalton Trans.*, 2016, **45**, 9669–9675.
5 W. Duan, M. Zhao, J. Shen, S. Zhao and X. Song, *Dalton Trans.*, 2017, **46**, 12019–12026.
6 J. Li, S.-H. Luo, Q. Wang, S. Yan, J. Feng, X. Ding, P. He and L. Zong, *J. Electrochem. Soc.*, 2019, **166**, A118–A124.
7 L. Zhu, L. Xie, C. Bao, X. Yan and X. Cao, *Int. J. Energy Res.*, 2019, **44**, 298–308.
8 L. Huan, S.-H. Luo, S.-X. Yan, Y.-F. Wang, Q. Wang, M.-Q. Li and Y.-H. Zhang, *J. Electroanal. Chem.*, 2019, **850**, 113434.
9 U.-H. Kim, L.-Y. Kuo, P. Kaghazchi, C. S. Yoon and Y.-K. Sun, *ACS Energy Lett.*, 2019, **4**, 576–582.
10 I. Lee, J. Kim, S. Han, J.-I. Park, J.-M. Lee, D.-H. Kim, S.-C. Nam and S. Yoon, *J. Electrochem. Soc.*, 2016, **163**, A1336–A1339.
11 A. Purwanto, C. S. Yudha, U. Ubaidillah, H. Widiyandari, T. Ogi and H. Haerudin, *Mater. Res. Express*, 2018, **5**, 122001.
12 C. T. Cherian, M. V. Reddy, S. C. Haur and B. V. R. Chowdari, *ACS Appl. Mater. Interfaces*, 2013, **5**, 918–923.
13 L. Linlin, P. Shengjie, C. Yanling, T. Peifen, W. Jin, W. Grace, K. Yahwen, W. Chuiling and S. Madhavi, *Chem.–Eur. J.*, 2013, **19**, 5892–5898.
14 M. V. Reddy, K. Y. H. Kenrick, T. Y. Wei, G. Y. Chong, G. H. Leong and B. V. R. Chowdari, *J. Electrochem. Soc.*, 2011, **158**, A1423.
15 Q. Xie, F. Li, H. Guo, L. Wang, Y. Chen, G. Yue and D. L. Peng, *ACS Appl. Mater. Interfaces*, 2013, **5**, 5508–5517.
16 J. Li, S. Xiong, Y. Liu, Z. Ju and Y. Qian, *ACS Appl. Mater. Interfaces*, 2013, **5**, 981–988.
17 C. Fu, G. Li, D. Luo, Q. Li, J. Fan and L. Li, *ACS Appl. Mater. Interfaces*, 2014, **6**, 15822–15831.
18 C. Fu, G. Li, D. Luo, X. Huang, J. Zheng and L. Li, *ACS Appl. Mater. Interfaces*, 2014, **6**, 2439–2449.
19 L. Li, Y. Cheah, Y. Ko, P. Teh and M. Srinivasan, *J. Mater. Chem. A*, 2013, **1**, 10935–10941.
20 J. Leng, Z. Wang, J. Wang, H. H. Wu, G. Yan, X. Li, H. Guo, Y. Liu, Q. Zhang and Z. Guo, *Chem. Soc. Rev.*, 2019, **48**, 3015–3072.
21 L. Tao, X. Li, Z. Wang and H. Guo, *J. Power Sources*, 2017, **342**, 495–503.
22 Y. Kim and D. Kim, *ACS Appl. Mater. Interfaces*, 2012, **4**, 586.
23 Q. Xie, W. Li and A. Manthiram, *Chem. Mater.*, 2019, **31**, 938–946.
24 K. He, Z. Ruan, X. Teng and Y. Zhu, *Mater. Res. Bull.*, 2017, **90**, 131–137.
25 L. Wen, O. Pilgun, L. Xien, L. Min-Joon, C. Woongrae, C. Sujong, K. Youngsik and C. Jaephil, *Angew. Chem.*, 2015, **54**, 4440–4457.
26 X. Zheng, X. Li, Z. Wang, H. Guo, Z. Huang, G. Yan and W. Ding, *Electrochim. Acta*, 2016, **191**, 832–840.
27 K. K. Lian, D. W. Kirk and S. J. Thorpe, *J. Electrochem. Soc.*, 1995, **142**, 4309.
28 A. M. Venezia, R. Bertoncello and G. Deganello, *Surf. Interface Anal.*, 2010, **23**, 239–247.
29 S. Y. Chong, H. H. Ryu, G. T. Park, J. H. Kim and Y. K. Sun, *J. Mater. Chem. A*, 2018, **6**, 4126–4132.
30 J. Zhao, Z. Wei, A. Huq, S. T. Misture, B. Zhang, S. Guo, L. Wu, Y. Zhu, Z. Chen and K. Amine, *Adv. Energy Mater.*, 2017, **7**, 1601266.
31 S. Deng, Y. Li, Q. Dai, J. Fu, Y. Chen, J. Zheng, T. Lei, J. Guo, J. Gao and W. Li, *Sustainable Energy Fuels*, 2019, **3**, 3234–3243.

32 Z. Huang, Z. Wang, Q. Jing, H. Guo, X. Li and Z. Yang, *Electrochim. Acta*, 2016, **192**, 120–126.
33 M. J. Zheng, J. Li, R. Z. Zhang, J. X. Guo and Y. Yang, *Solid State Ionics*, 2008, **179**, 1794–1799.
34 T. Lei, Y. Li, Q. Su, G. Cao, W. Li, Y. Chen, L. Xue and S. Deng, *Ceram. Int.*, 2018, **44**, 8809–8817.
35 D. H. Jeon, *Energy Storage Mater.*, 2019, **18**, 139–147.
36 L. Yanguang, T. Bing and W. Yiying, *Nano Lett.*, 2008, **8**, 265–270.
37 J. Zhu, G. Cao, Y. Li, S. Wang, S. Deng, J. Guo, Y. Chen, T. Lei, J. Zhang and S. Chang, *Electrochim. Acta*, 2019, **325**, 134889.
38 H. Lu, H. Zhou, A. M. Svensson, A. Fossdal, E. Sheridan, S. Lu and F. Vullum-Bruer, *Solid State Ionics*, 2013, **249–250**, 105–111.
39 M. Wohlfahrt-mehrens, C. Vogler and J. Garche, *J. Power Sources*, 2004, **127**, 58–64.
40 H. Zheng, Q. Sun, L. Gao, X. Song and V. S. Battaglia, *J. Power Sources*, 2012, **207**, 134–140.
41 S. T. Myung, K. Izumi, S. Komaba, Y. K. Sun, H. Yashiro and N. Kumagai, *Chem. Mater.*, 2005, **17**, 3695–3704.
42 C. H. Jo, D. H. Cho, H. J. Noh, H. Yashiro, Y. K. Sun and S. Myung, *Nano Res.*, 2015, **9**, 1464–1479.
43 J. R. Macdonald, *Solid State Ionics*, 2005, **176**, 1961–1969.